

# RE-ACCELERATION MODEL FOR THE “TOOTHBRUSH” RADIO RELIC

HYESUNG KANG

Department of Earth Sciences, Pusan National University, Pusan 609-735, Korea; [hskang@pusan.ac.kr](mailto:hskang@pusan.ac.kr)

Received March 20, 25; accepted April \*\*, 2016

**Abstract:** The Toothbrush radio relic associated the merging cluster 1RXS J060303.3 is presumed to be produced by relativistic electrons accelerated at merger-driven shocks. Since the shock Mach number inferred from the observed radio spectral index,  $M_{\text{radio}} \approx 2.8$ , is larger than that estimated from X-ray observations,  $M_{\text{X-ray}} \lesssim 1.5$ , we consider the re-acceleration model in which a weak shock of  $M_s \approx 1.2 - 1.5$  sweeps through the intracluster plasma with a preshock population of relativistic electrons. We find the models with a power-law momentum spectrum with the slope,  $s \approx 4.6$ , and the cutoff Lorentz factor,  $\gamma_{e,c} \approx 7 - 8 \times 10^4$  can reproduce reasonably well the observed profiles of radio fluxes and integrated radio spectrum of the head portion of the Toothbrush relic. This study confirms the strong connection between the ubiquitous presence of fossil relativistic plasma originated from AGNs and the shock-acceleration model of radio relics in the intracluster medium.

**Key words:** acceleration of particles — cosmic rays — galaxies: clusters: general — shock waves

## 1. INTRODUCTION

Some galaxy clusters contain diffuse radio sources on the scales as large as  $\sim 2$  Mpc, called ‘radio relics’ (e.g., Feretti et al. 2012; Brüggén et al. 2012; Brunetti & Jones 2014). They could be classified into two main groups according to their origins and properties (Kempner et al. 2004). *AGN relics/Radio phoenix* are thought to originate from AGNs. AGN relics are radio-emitting relativistic plasma left over from jets and lobes of extinct AGNs, and eventually turn into ‘radio ghosts’ when the electron plasma becomes radio-quiet due to synchrotron and inverse Compton (iC) energy losses (Ensslin 1999). Radio ghosts can be reborn as *radio phoenix*, if cooled electrons with the Lorentz factor  $\gamma_e \lesssim 100$  are compressed and re-energized to  $\gamma_e \sim 10^4$  by the structure formations shocks (Ensslin & Gopal-Krishna 2001). AGN relics/Radio phoenix typically have roundish shapes and steep-curved integrated spectra of aged electron populations, and they are found near their source AGN (e.g., Slee et al. 2001; van Weeren et al. 2011; Clarke et al. 2013; de Gasperin et al. 2015). *Radio gischt* relics, on the other hand, are thought to be produced via Fermi first order process at merger-driven shock waves in the intracluster medium (ICM). They show thin elongated morphologies, spectral steepening downstream of the putative shock, integrated radio spectra with a power-law form, and high polarization level (Ensslin et al. 1998; van Weeren et al. 2010).

Most of the observed features of radio *gischt* relics can be adequately explained by diffusive shock acceleration (DSA) model in which relativistic electrons are (re-)accelerated at shock waves: (1) gradual spectral steepening across the relic width, (2) power-law-like integrated spectrum with the spectral index that

is larger by 0.5 than the spectral index at the relic edge, i.e.,  $\alpha_{\text{int}} \sim \alpha_{\text{shock}} + 0.5$ , and (3) high polarization level up to 50 % that is expected from the shock compression of turbulent magnetic fields (e.g., van Weeren et al. 2010; Brunetti & Jones 2014). Moreover, it is now well accepted from both observational and theoretical studies that the cosmological shocks are ubiquitous in the ICM and nonthermal particles can be accelerated at such shocks via the DSA process (e.g., Ryu et al. 2003; Vazza et al. 2009; Skillman et al. 2011; Hong et al. 2014).

Yet there remain some puzzles in the DSA origin of radio *gischt* relics such as low acceleration efficiency of weak shocks and low frequency of merging clusters with detected radio relics. The structure formation shocks with high kinetic energy fluxes, especially those induced by cluster mergers, are thought to have small Mach numbers of  $M_s \lesssim 3$  (Ryu et al. 2003; Vazza et al. 2009), while the DSA efficiency at such weak shocks is expected to be extremely low (Kang & Ryu 2011). In particular, it is not well understood how seed electrons are injected into the Fermi first order process at weak shocks that form in the high-beta ( $\beta = P_{\text{gas}}/P_{\text{mag}} \sim 100$ ) ICM plasma (e.g., Kang et al. 2014). According to structure formation simulations, the mean separation between shock surfaces in the ICM is about 1 Mpc (Ryu et al. 2003). Then several shocks and associated radio relics could be present in merging clusters, if every shock were to produce relativistic electrons. Yet only  $\sim 10$  % of luminous merging clusters are observed to host radio relics (Feretti et al. 2012). Furthermore, in some clusters a shock is detected in X-ray observations without associated diffuse radio sources (e.g., Russell et al. 2011).

In order to solve these puzzles re-acceleration of fossil electrons pre-existing in the ICM was proposed by several authors (e.g., Kang & Ryu 2011; Kang et al. 2012;

Pinzke et al. 2013). The presence of radio galaxies, AGN relics and radio phoenix implies that the ICM may host radio-quiet ghosts of fossil electrons (Kang & Ryu 2016). In addition, fossil electrons can be produced by previous episodes of shocks and turbulence that are induced by merger-driven activities. Since fossil electrons with  $\gamma_e \gtrsim 100$  can provide seed electrons to the DSA process and enhance the acceleration efficiency, they will alleviate the low acceleration efficiency problem of weak ICM shocks. Moreover, the re-acceleration scenario may explain the low occurrence of radio relics among merging clusters, since the ICM shocks can light up as radio relics only when they encounter clouds of fossil electrons (Kang & Ryu 2016).

The giant radio relic found in the merging cluster 1RXS J060303.3, the so-called “Toothbrush” relic is a typical example of radio gischt relics. It has a peculiar linear morphology with multiple components that look like the head and handle of a toothbrush (van Weeren et al. 2012). Recently, van Weeren et al. (2016) reported that the spectral index at the northern edge of B1 relic (the head portion of the Toothbrush) is  $\alpha_{\text{sh}} \approx 0.8$  with the corresponding radio Mach number,  $M_{\text{radio}} \approx 2.8$  (see Equation 1). But the gas density jump around B1 inferred from X-ray observations implies a much weaker shock with  $M_{\text{X-ray}} \approx 1.2 - 1.5$ . This discrepancy between  $M_{\text{radio}}$  and  $M_{\text{X-ray}}$  can be explained, if a pre-existing population of relativistic electrons has the right power-law slope, i.e.,  $f_{\text{up}}(p) \propto p^{-4.6}$ .

In this study, we attempt to explain the observed properties of relic B1 by the re-acceleration model in which a low Mach number shock ( $M_s \approx 1.2 - 1.5$ ) sweeps through a cloud of pre-existing relativistic electrons. In the next section, we explain some basic physics of the DSA model, while the numerical simulations and the shock models are described in Section 3. The comparison of our results with observations is discussed in Section 4. A brief summary is given in Section 5.

## 2. DSA MODEL

### 2.1. Electron and Radiation Spectra of Radio Relics

According to the DSA model for a *steady planar* shock, the electrons that are injected and accelerated at a shock of the sonic Mach number  $M_s$  form a power-law momentum distribution function,  $f_e(p, r_s) \propto p^{-q}$  with the slope  $q = 4M_s^2/(M_s^2 - 1)$  (Drury 1983). Then the electron spectrum integrated over the downstream region of the shock steepens by one power of momentum, i.e.,  $F_e(p) \propto p^{-(q+1)}$  due to synchrotron and iC cooling (Ensslin et al. 1998).

The radio synchrotron spectrum radiated by those electrons becomes a power-law of  $j_\nu(r_s) \propto \nu^{-\alpha_{\text{sh}}}$  at the shock position with the ‘shock’ index

$$\alpha_{\text{sh}} = \frac{(q-3)}{2} = \frac{(M_s^2+3)}{2(M_s^2-1)}. \quad (1)$$

This relation is often used to infer the Mach number

of the putative shock,  $M_{\text{radio}}$ , from the radio spectral index. Moreover, the volume-integrated radio spectrum behind the shock becomes another steepened power-law,  $J_\nu \propto \nu^{-A_\nu}$  with the ‘integrated’ index  $A_\nu = \alpha_{\text{sh}} + 0.5$  above the break frequency  $\nu_{\text{br}}$ . Note that the break frequency depends on the magnetic field strength,  $B$ , and the shock age,  $t_{\text{age}}$ , as follows:

$$\nu_{\text{br}} \approx 0.63 \text{GHz} \left( \frac{t_{\text{age}}}{100 \text{Myr}} \right)^{-2} \left[ \frac{(5 \mu\text{G})^2}{B^2 + B_{\text{rad}}^2} \right]^2 \left( \frac{B}{5 \mu\text{G}} \right), \quad (2)$$

where  $B_{\text{rad}} = 3.24 \mu\text{G}(1+z)^2$  and  $B$  is expressed in units of  $\mu\text{G}$  (Kang 2011).

However, such expectation for simple power-law spectra needs to be modified in real observations. If the break frequency  $\nu_{\text{br}}$  lies in the range of observation frequencies (typically  $0.1 \lesssim \nu_{\text{obs}} \lesssim 10 \text{GHz}$ ), for instance, the integrated radio spectrum steepens gradually over  $\sim (0.1 - 10)\nu_{\text{br}}$ , instead of forming a single power-law (Kang 2015a). Furthermore, in the case of spherically expanding shocks with varying speeds, both the electron spectrum and the ensuing radio spectrum exhibit spectral curvatures (Kang 2015b). In fact, the spectral steepening above  $\sim 2 \text{GHz}$  have been detected in the relic in A2256 (Trasatti et al. 2015) and the Sausage relic in CIZA J2242.8+5301 (Stroe et al. 2016). The integrated spectral index of B1 of the Toothbrush relic increases from  $A_\nu \approx 1.0$  below 2.5 GHz to  $A_\nu \approx 1.4$  above 2.0 GHz (Stroe et al. 2016).

In the re-acceleration model, on the other hand, the re-accelerated electron spectrum must depend on the shape of the initial spectrum of pre-existing electrons (e.g., Kang & Ryu 2015). For the preshock electron population of a power-law form,  $f_{\text{up}} \propto p^{-s}$ , for example, the ensuing radio spectrum at the shock position can have  $\alpha_{\text{sh}} \leq (s-3)/2$  or  $\alpha_{\text{sh}} \leq (q-3)/2$ , depending on  $s$ ,  $q$ , and observation frequencies (Kang & Ryu 2016). Hence, in the re-acceleration model, the Mach number of the putative shock cannot be inferred directly from the radio spectral index, based on the expectation of the simple version of DSA model. This may explain the fact that in some radio relics such as the Toothbrush relic, the radio Mach number,  $M_{\text{radio}}$ , estimated from the radio spectral index does not agree with the X-ray Mach number,  $M_{\text{X-ray}}$ , estimated from the discontinuities in X-ray observations (e.g., Akamatsu & Kawahara 2013).

### 2.2. Width of Radio Relics

The cluster RX J0603.3+4214 that hosts the Toothbrush relic is located at the redshift  $z = 0.225$  (van Weeren et al. 2012). According to the recent observational study of van Weeren et al. (2016), FWHMs of B1 relic at 150 MHz and 610 MHz are about 140 kpc and 110 kpc, respectively, and the spectral index between these two frequencies,  $\alpha_{0.15}^{0.61}$  increases from 0.8 at the northern edge of B1 to 1.9 at  $\sim 200 \text{kpc}$  toward the cluster center. The width of B1 relic at 610 MHz is about 2 times larger than the FWHM  $\sim 55 \text{kpc}$  of the Sausage relic at 630 MHz (van Weeren et al. 2010).

In the postshock region, accelerated electrons lose energy via synchrotron emission and inverse Compton scattering off the cosmic background radiation in the following time scale:

$$t_{\text{rad}}(\gamma_e) = 9.8 \times 10^7 \text{ yr} \left[ \frac{(5 \mu\text{G})^2}{B^2 + B_{\text{rad}}^2} \right]^2 \left( \frac{\gamma_e}{10^4} \right)^{-1} \quad (3)$$

(Kang 2011). For low energy electrons, the physical width of the postshock volume of radio-emitting electrons is simply determined by the advection length,  $\Delta l_{\text{adv}} \approx u_2 \cdot t_{\text{age}}$ , where  $u_2$  is the downstream flow speed. For high energy electrons, on the other hand, it becomes the cooling length,  $\Delta l_{\text{cool}}(\gamma_e) \approx u_2 \cdot t_{\text{rad}}(\gamma_e)$ . So the width of the radio-emitting shell of electrons with  $\gamma_e$  is  $\Delta l(\gamma_e) = \min[\Delta l_{\text{cool}}(\gamma_e), \Delta l_{\text{adv}}]$ .

In order to connect the spatial distribution of electrons with that of radio emission, one can use the fact that the synchrotron emission from mono-energetic electrons with  $\gamma_e$  peaks around

$$\nu_{\text{peak}} \approx 0.63 \text{ GHz} \cdot \left( \frac{B}{5 \mu\text{G}} \right) \left( \frac{\gamma_e}{10^4} \right)^2, \quad (4)$$

along with the relation between the observation frequency and the source frequency,  $\nu_{\text{obs}} = \nu_{\text{peak}}/(1+z)$ . For low frequency radio emission emitted by uncooled, low energy electrons, the width of radio relics becomes similar to the advection length:

$$\Delta l_{\text{low}} \approx 100 \text{ kpc} \cdot u_{2,3} \cdot \left( \frac{t_{\text{age}}}{100 \text{ Myr}} \right), \quad (5)$$

where  $u_{2,3} = u_2/10^3 \text{ km s}^{-1}$ .

For high frequency emission radiated by cooled high energy electrons, the relic width would be similar to the cooling length (Kang & Ryu 2015):

$$\Delta l_{\text{high}} \approx 100 \text{ kpc} \cdot W \cdot u_{2,3} \cdot Q \cdot \left[ \frac{\nu_{\text{obs}}(1+z)}{0.63 \text{ GHz}} \right]^{-1/2}. \quad (6)$$

Here the factor  $W \sim 1.2 - 1.3$  takes account for the fact that the spatial distribution of synchrotron emission at  $\nu_{\text{peak}}$  is somewhat broader than that of electrons with the corresponding  $\gamma_e$ , because more abundant, lower energy electrons also make contributions (Kang 2015a). The factor  $Q$  is defined as

$$Q(B, z) \equiv \left[ \frac{(5 \mu\text{G})^2}{B^2 + B_{\text{rad}}(z)^2} \right] \left( \frac{B}{5 \mu\text{G}} \right)^{1/2}, \quad (7)$$

where again  $B$  and  $B_{\text{rad}}$  must be expressed in units of microgauss. Figure 1 shows that  $Q$  evaluated for  $z = 0.225$  peaks at  $B \approx 2.8 \mu\text{G}$ . Note that for a given value  $Q$  there are two possible values of  $B$  that satisfies Equation (7).

For B1 relic in the Toothbrush cluster, the estimated downstream speed is  $u_2 \approx 1.1 \times 10^3 \text{ km s}^{-1}$ , if we take the following observation data:  $kT_1 \sim 6 - 7 \text{ keV}$  and  $M_s \sim 1.3 - 1.5$  (van Weeren et al. 2016). So if we adopt

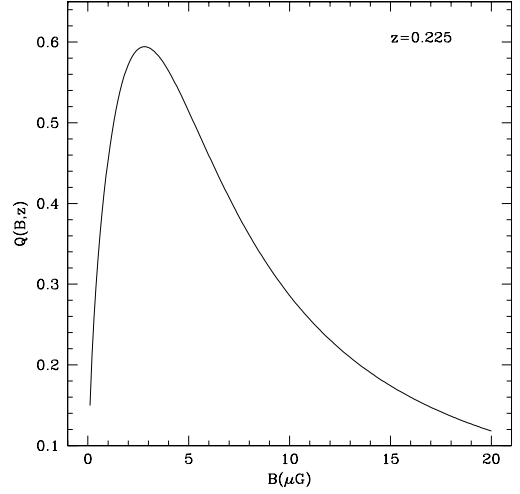


**Figure 1.** The factor  $Q(B, z)$  for  $z = 0.225$  given in Equation (7).

$W \approx 1.3$ ,  $u_{2,3} \approx 1.1$ , and  $t_{\text{age}} \approx 110 \text{ Myr}$ , then the width of low-frequency radio emission in a *planar* shock becomes  $\Delta l_{\text{low}} \approx 120 \text{ kpc}$ . On the other hand, at high frequencies, for example, at  $\nu_{\text{obs}} = 630 \text{ MHz}$  it becomes only  $\Delta l_{\text{high}} \approx 78 \text{ kpc}$  for the largest value  $Q_{\text{max}} \approx 0.6$  (with  $B \approx 2.8 \mu\text{G}$ ).

As shown in Figure 2, the projected relic width of a spherical shell can be larger than  $\Delta l_{\text{low}}$  or  $\Delta l_{\text{high}}$ , if the arc-like partial shell (marked in blue) is tilted with respect to the sky plane (dashed line). On the other hand, if the shell were to be viewed almost face-on, the spectral index  $\alpha$  would be roughly constant across the width of the relic, which is in contradiction with observations (van Weeren et al. 2016). Later we will consider models with the various projection angles,  $-5^\circ \leq \psi_1 \leq +15^\circ$  and  $0^\circ \leq \psi_2 \leq +35^\circ$ .

### 3. NUMERICAL CALCULATIONS

The numerical setup and physical models for DSA simulations were described in details in Kang (2015b). So only basic features are given here.

#### 3.1. DSA Simulations for 1D Spherical Shocks

We follow time-dependent diffusion-convection equation for the pitch-angle-averaged phase space distribution function for CR electrons,  $f_e(r, p, t) = g_e(r, p, t)p^{-4}$ , in the one-dimensional (1D) spherically symmetric geometry:

$$\begin{aligned} \frac{\partial g_e}{\partial t} + u \frac{\partial g_e}{\partial r} &= \frac{1}{3r^2} \frac{\partial(r^2 u)}{\partial r} \left( \frac{\partial g_e}{\partial y} - 4g_e \right) \\ &+ \frac{1}{r^2} \frac{\partial}{\partial r} \left[ r^2 D(r, p) \frac{\partial g_e}{\partial r} \right] + p \frac{\partial}{\partial y} \left( \frac{b}{p^2} g_e \right), \end{aligned} \quad (8)$$

where  $u(r, t)$  is the flow velocity,  $y = \ln(p/m_e c)$ ,  $m_e$  is the electron mass, and  $c$  is the speed of light (Skilling 1975). Here  $r$  is the radial distance from the center

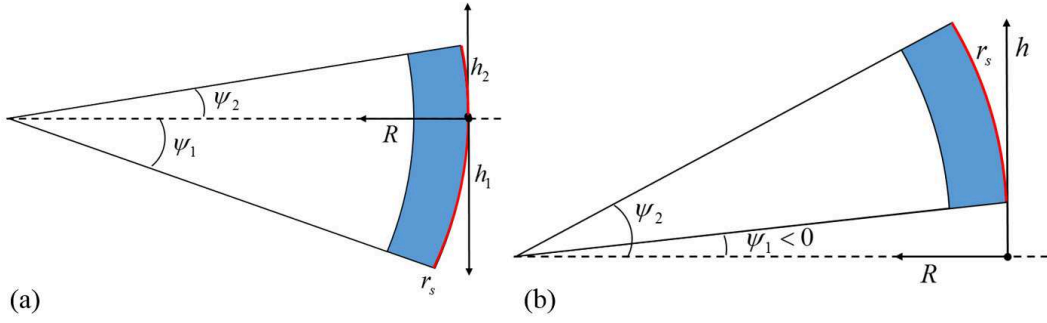


**Figure 2.** Two geometrical configurations of the radio-emitting volume (marked in blue) downstream of a spherical shock at  $r_s$  (marked in red) for the Toothbrush relic.

of the spherical coordinate, which assumed to coincide with the cluster center. We assume a Bohm-like spatial diffusion coefficient,  $D(r, p) \propto p/B$ . The cooling term  $b(p) = -dp/dt = -p/t_{\text{rad}}$  accounts for electron synchrotron and iC losses. The test-particle version of CRASH (Cosmic-Ray Amr SHock) code in a co-moving 1D spherical grid is used to solve Equation (8) (Kang & Jones 2006).

### 3.2. Models for Magnetic Fields

We consider simple yet physically motivated models for the postshock magnetic fields as in Kang (2015b): (1) the magnetic field strength across the shock transition is assumed to increase due to compression of the two perpendicular components,

$$B_2(t) = B_1 \sqrt{1/3 + 2\sigma(t)^2/3}, \quad (9)$$

where  $B_1$  and  $B_2$  are the preshock and postshock magnetic field strengths, respectively, and  $\sigma(t) = \rho_2/\rho_1$  is the density compression ratio across the shock. (2) for the downstream region ( $r < r_s$ ), the magnetic field strength is assumed to scale with the gas pressure:

$$B_{\text{dn}}(r, t) = B_2(t) \cdot [P_g(r, t)/P_{g,2}(t)]^{1/2}, \quad (10)$$

where  $P_{g,2}(t)$  is the gas pressure immediately behind the shock.

### 3.3. Preshock Electron Population

Several possible origins for pre-existing, relativistic electron populations in the ICMs can be considered: (1) old remnants of radio jets from AGNs (radio ghosts), (2) electron populations that were accelerated by previous shocks, and (3) electron populations that were accelerated by turbulence during merger activities (e.g., Kang & Ryu 2015). In the case of the Toothbrush relic, van Weeren et al. (2016) suggested that the AGN located at the southwestern end of B1 relic might be the candidate source that supplies relativistic plasmas to this relic.

Here we assume that a preshock population of electrons has a power-law spectrum with exponential cutoff as follows:

$$f_{\text{up}}(p) \propto p^{-s} \exp \left[ - \left( \frac{\gamma_e}{\gamma_{e,c}} \right)^2 \right], \quad (11)$$

where  $s = 4.6$  is chosen to match the observed shock index,  $\alpha_{\text{sh}} \approx 0.8$ . We consider several models with a range of the cutoff Lorentz factor,  $\gamma_{e,c} = 2 - 10 \times 10^4$ , and find that  $\gamma_{e,c} \sim 7 - 8 \times 10^4$  produces the best match to the observations of both Stroe et al. (2016) and van Weeren et al. (2016).

Note that this preshock electron population could be detected in radio, as can be seen in Figure 3, since  $\gamma_{e,c}$  is quite high. However, no radio fluxes have been detected north of the northern edge of B1 (the shock location) (van Weeren et al. 2016). Since the candidate AGN is located about 200 kpc downstream of the shock location, it is possible that the shock has almost sweeps through the upstream region with these preshock electrons emitted by the AGN.

In order to isolate the effects of the pre-existing population, the *in situ* injection at the shock is turned off in the DSA simulations presented here.

### 3.4. Shock parameters

The shock parameters are chosen to emulate roughly the shock associated with B1 relic in the Toothbrush cluster. According to van Weeren et al. (2016),  $kT_1 = 8.3^{+3.2}_{-2.4}$  keV and  $kT_2 = 8.2^{+0.7}_{-0.9}$  keV across B1, so the postshock temperature is better constrained compared to the preshock temperature. Considering that  $\Delta l_{\text{high}}$  is smaller the observed width ( $\sim 110$  kpc) at 610 MHz, we choose a higher value of  $kT_2 = 8.9$  keV in order to maximize  $\Delta l_{\text{high}}$ . Then we consider two values of the initial Mach number, which determine the preshock temperature and the initial shock speed as follows:

(1)  $M_{s,i} = 1.3$ ,  $kT_1 = 6.9$  keV,  $u_{s,i} = 1.8 \times 10^3$  km s $^{-1}$ , and  $\gamma_{e,c} = 8.0 \times 10^4$ .

(2)  $M_{s,i} = 1.5$ ,  $kT_1 = 5.9$  keV,  $u_{s,i} = 1.9 \times 10^3$  km s $^{-1}$ , and  $\gamma_{e,c} = 7.0 \times 10^4$ .

The spherical shock slows down to  $M_s \approx 1.2$  in the  $M_{s,i} = 1.3$  model and  $M_s \approx 1.4$  in the  $M_{s,i} = 1.5$  model at the shock age of  $t_{\text{age}} \approx 110$  Myr. The preshock magnetic field strengths is assumed to be  $B_1 = 2 \mu\text{G}$ , resulting in the postshock strength,  $B_2 = 2.5 - 2.8 \mu\text{G}$ .

The density of the background gas in the cluster outskirts is assumed to decrease as  $\rho_{\text{up}} = \rho_0(r/r_{s,i})^{-2}$ . This corresponds to the so-called beta model for isothermal ICMs,  $\rho(r) \propto [1 + (r/r_c)^2]^{-3\beta/2}$  with  $\beta \sim 2/3$  (Sarazin 1988).

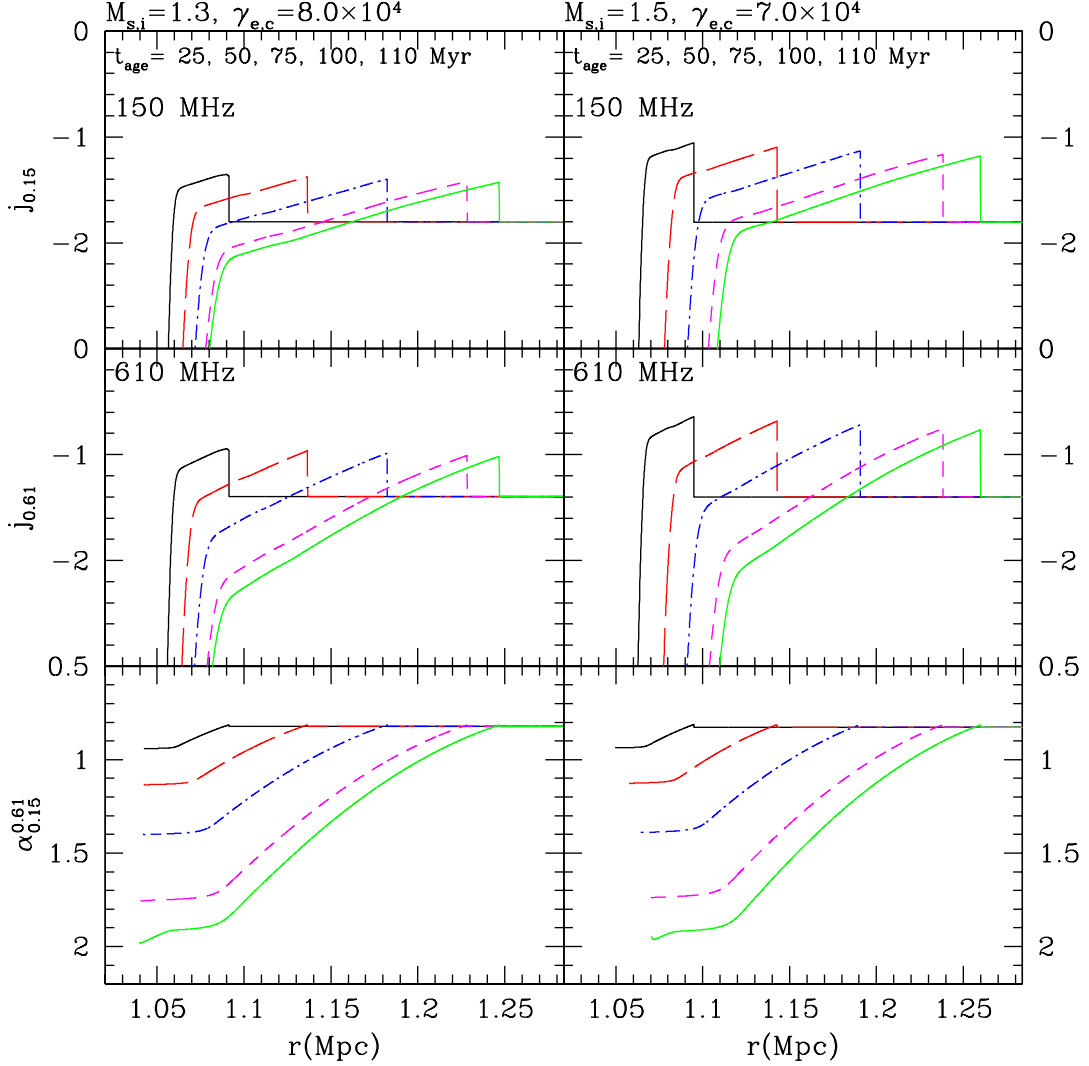


**Figure 3.** Time Evolution of the synchrotron emissivity,  $j_\nu(r)$  at 150 MHz (top panels) and 610 MHz (middle), and the spectral index,  $\alpha_{0.15}^{0.61}$  between 150 and 610 MHz (bottom) plotted as a function of the radial distance from the cluster center,  $r(\text{Mpc})$ , in the two models with the initial Mach number  $M_{s,i} = 1.3$  (left panels) and  $M_{s,i} = 1.5$  (right panels). The results at 25 (black solid lines), 50 (red long dashed), 75 (blue dot-dashed), 100 (magenta dashed), and 110 Myr (green solid) are presented.

#### 4. RESULTS OF DSA SIMULATIONS

Figure 3 shows the synchrotron emissivity,  $j_\nu(r)$  at 150 MHz and 610 MHz, and the spectral index,  $\alpha_{0.15}^{0.61}$  between the two frequencies in the models with  $M_{s,i} = 1.3$  and  $M_{s,i} = 1.5$ . It illustrates how the downstream radio-emitting region broadens in time as the spherical shock moves outward away from the cluster center, and how the radio spectrum steepens behind the shock further in time. In the model with  $M_{s,i} = 1.3$ , the emissivities at both frequencies increase by a factor of 2.4–2.7 across the shock, while they increase by a factor of 4.3–5.6 in the model with  $M_{s,i} = 1.5$ . Again note that no radio fluxes have been detected in the upstream region of B1 relic (van Weeren et al. 2016). In that regard, the  $M_{s,i} = 1.5$  model might be preferred, since it has a larger amplification factor across the shock.

The emissivity  $j_{0.61}(r)$  decreases much faster than  $j_{0.15}(r)$  behind the shock, since the cooling length of higher energy electrons is shorter than that of lower energy electrons. The spectral index at the shock is  $\alpha_{0.15}^{0.61} \approx 0.8$ , since the slope of the pre-existing electron population is  $s = 4.6$  in Equation (11). It increases to  $\alpha_{0.15}^{0.61} \approx 1.9$  at the far downstream regions, which is in good agreement with observations.

Note that in the shock rest frame the postshock flow speed,  $u_{\text{dn}}(r, t)$ , increases behind spherically expanding shocks, so the advection length is larger than that estimated for planar shocks. According to Figure 3, at the shock age of 110 My, for instance, the advection lengths become  $\sim 150 - 160$  kpc, while  $\Delta l_{\text{low}} \approx 120$  kpc estimated for planar shocks.

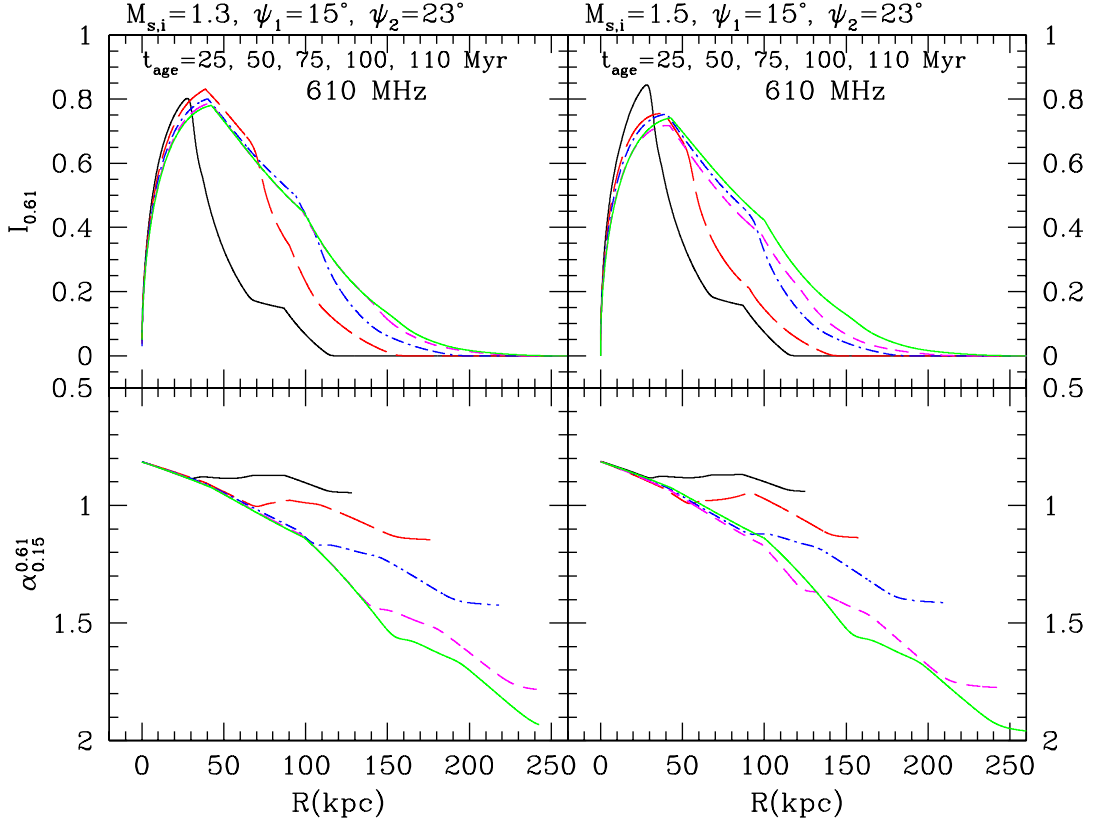


**Figure 4.** Time Evolution of the surface brightness  $I_\nu$  at 610 MHz (top panels) and the spectral index,  $\alpha_{0.15}^{0.61}$  between 150 and 610 MHz plotted as a function of the projected distance behind the shock,  $R$ (kpc), in the two models with the initial Mach number  $M_{s,i} = 1.3$  (left panels) and  $M_{s,i} = 1.5$  (right panels). The projection angles are assume to be  $\psi_1 = 15^\circ$  and  $\psi_2 = 23^\circ$ . The results at 25 (black solid lines), 50 (red long dashed), 75 (blue dot-dashed), 100 (magenta dashed), and 110 Myr (green solid) are presented.

#### 4.1. Surface Brightness and Spectral Index Profiles

The radio surface brightness,  $I_\nu(R)$ , is calculated from the emissivity  $j_\nu(r)$  by adopting the same geometric volume of radio-emitting electrons as in Figure 1 of Kang (2015b). Here  $R$  is the distance behind the projected shock edge in the plane of the sky, while  $r$  is the radial distance from the cluster center. As shown in Figure 2, the various projection angles  $\psi_1 + \psi_2 = 30^\circ - 45^\circ$  are considered in order to explore the projection effects. For example, if both  $\psi_1 > 0$  and  $\psi_2 > 0$ , the surface brightness is calculated as follow:

$$I_\nu(R) = \int_0^{h_{1,\max}} j_\nu(r) dh_1 + \int_0^{h_{2,\max}} j_\nu(r) dh_2, \quad (12)$$

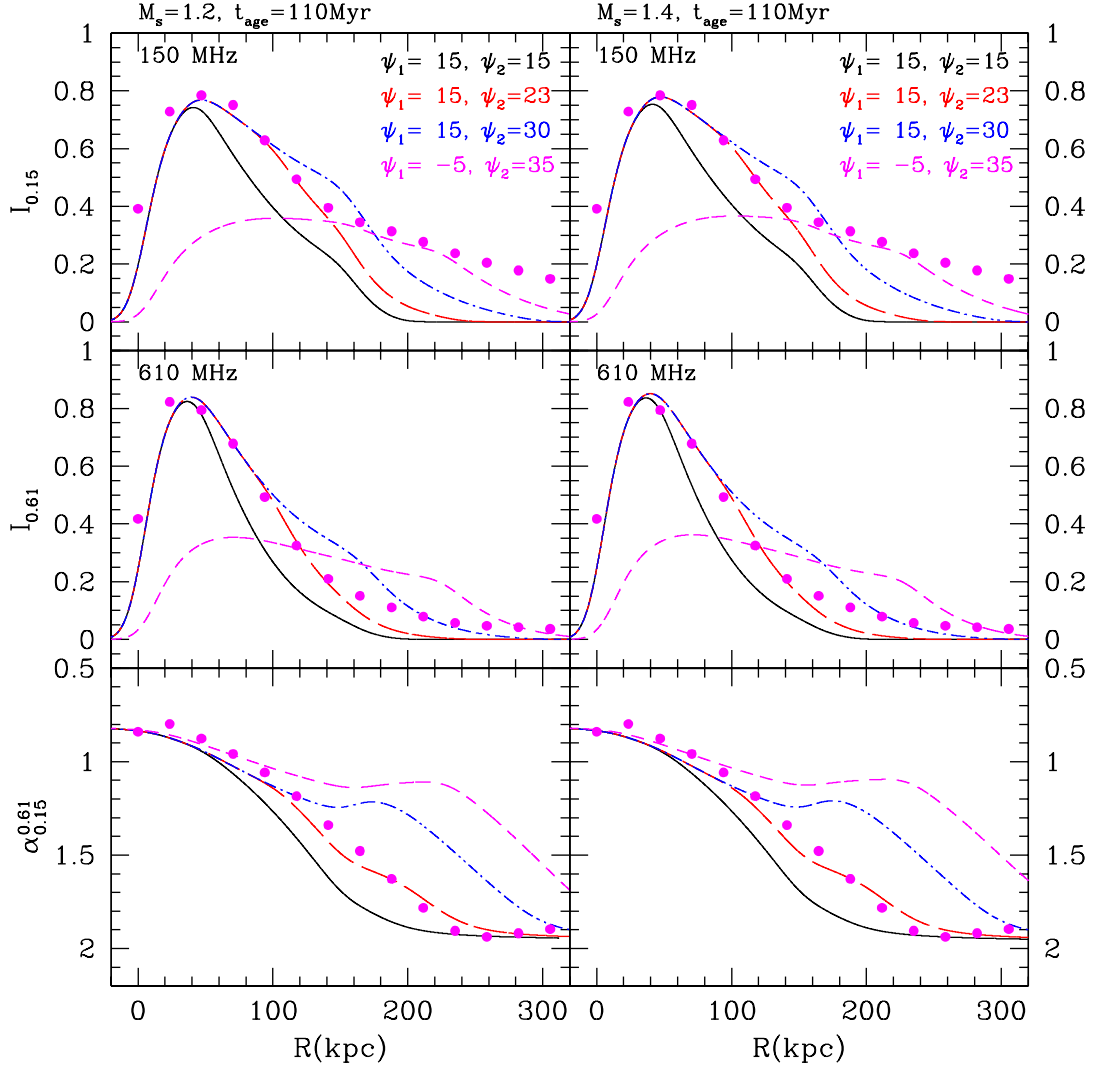
where  $h$  is the path length along line of sights. Note that the radio flux density,  $S_\nu$ , can be obtained by convolving  $I_\nu$  with a telescope beam as  $S_\nu(R) \approx I_\nu(R) \pi \theta_1 \theta_2 (1+z)^{-3}$ , if the brightness distribution is broad compared to the beam size of  $\theta_1 \theta_2$ . In addition, the spectral index,  $\alpha_{0.15}^{0.61}$  is calculated from the projected  $I_\nu(R)$  at 150 and 610 MHz.

Figure 4 shows how  $I_\nu(R)$  at 610 MHz and  $\alpha_{0.15}^{0.61}$  evolve during 110 Myr in the two shock models. The

projection angles,  $\psi_1 = 15^\circ$  and  $\psi_2 = 23^\circ$ , are chosen to match the observed profiles of  $I_\nu(R)$  and  $\alpha_{0.15}^{0.61}$ , as shown in Figure 5. The shock has weakened to  $M_s \approx 1.2$  in the  $M_{s,i} = 1.3$  model and  $M_s \approx 1.4$  in the  $M_{s,i} = 1.5$  model at 110 Myr. In the early stage the relic width increases roughly with time. But it asymptotes to the cooling lengths in time, since the cooling of high energy electrons begins to control the width at later time.

The gradient of  $\alpha_{0.15}^{0.61}$  increases in time as postshock electrons loose energies. At  $t_{\text{age}} = 110$  My, the spectral index increases from  $\alpha_{0.15}^{0.61} \approx 0.8$  at the shock location to  $\alpha_{0.15}^{0.61} \approx 1.9$  about 230 kpc downstream of the shock in the two models. Note that the evolution of  $\alpha_{0.15}^{0.61}$  depends on the cutoff energy of the pre-existing electron populations. In order to obtain the observed profile that steepens from 0.8 to 1.9 over 230 kpc, we should choose  $\gamma_{e,c} \approx 8.0 \times 10^4$  for  $M_{s,i} = 1.3$  model and  $\gamma_{e,c} \approx 7.0 \times 10^4$  for  $M_{s,i} = 1.5$  model.

We find that the best fits to the observations of van Weeren et al. (2016) are obtained at 110 Myr for both models. Figure 5 shows  $I_\nu(R)$  at 150 and 610 MHz and  $\alpha_{0.15}^{0.61}$  at  $t_{\text{age}} = 110$  Myr for different sets of  $\psi_1$  and  $\psi_2$ . Note that Gaussian smoothing with  $6.5''$  resolution



**Figure 5.** Surface brightness  $I_\nu$  at 150 MHz (top panels) and at 610 MHz (middle panels), and the spectral index  $\alpha_{0.15}^{0.61}$  between the two frequencies (bottom panels) plotted as a function of projected distance behind the shock,  $R(\text{kpc})$ , for the shock models with  $M_s = 1.2$  (left panels) and  $M_s = 1.4$  (right panels) at  $t_{\text{age}} = 110 \text{ Myr}$ . The projection angles,  $\psi_1$  and  $\psi_2$ , for different curves are given in the plot. Gaussian smoothing with  $6.5''$  resolution ( $= 23.5 \text{ kpc}$ ) is applied in order to emulate radio observations. The magenta dots are the observational data of van Weeren et al. (2016).

( $= 23.5 \text{ kpc}$ ) is applied in order to emulate radio observations. The scales of  $I_\nu(R)$  are rescaled in arbitrary units. If we were to attempt to match the observed profile of  $I_{0.15}$  up to  $\sim 300 \text{ kpc}$ , then one of the projection angles should be larger than  $35^\circ$ , as can be seen in the top panels. With such projection angles, however, the predicted profile of  $\alpha_{0.15}^{0.61}$  would become much flatter than the observed profile. Since the observed radio fluxes could be contaminated by the halo components, we try to fit the observed profiles only for  $R < 150 \text{ kpc}$ . As can be seen in the figure, the model with  $\psi_1 = 15^\circ$  and  $\psi_2 = 23^\circ$  gives the best match to the observations. At  $110 \text{ Myr}$  the shock radius is  $r_s(t) \approx 1.25 - 1.26 \text{ Mpc}$  (see Figure 3). Note that in fitting the profile of  $I_\nu(R)$  with  $\psi_1 = 15^\circ$  and  $\psi_2 = 23^\circ$ ,  $r_s(t)(1 - \cos \psi_1) \approx 43 \text{ kpc}$  is related with the peak position at  $\sim 47 \text{ kpc}$ , while

$r_s(1 - \cos \psi_2) \approx 100 \text{ kpc}$  is related with the relic width of  $\sim 110 - 140 \text{ kpc}$ .

#### 4.2. Integrated Spectrum

As described in Section 2.1, the volume integrated radiation spectrum of a typical cluster shock with  $t_{\text{age}} \sim 100 \text{ Myr}$  is expected to steepen from  $\alpha_{\text{sh}}$  to  $\alpha_{\text{sh}} + 0.5$  gradually over  $0.1 - 10 \text{ GHz}$ . In the re-acceleration model, however, it also depends on the spectral shape of the preshock electron population. So the spectral curvature of the observed spectrum can be reproduced by adjusting the set of model parameters, i.e.,  $M_s$ ,  $B_1$ ,  $t_{\text{age}}$ ,  $s$  and  $\gamma_{e,c}$  in our models.

Figure 6 shows the time evolution of the integrated spectrum,  $J_\nu$ , during  $110 \text{ Myr}$  in the two shock models. The magenta dots show the observational data taken



from Table 3 of Stroe et al. (2016), which are rescaled to fit the simulated spectrum near 1 GHz by eye. We find that  $\gamma_{e,c} = 7 - 8 \times 10^4$  is needed in order to reproduce  $J_\nu$  both near 1 GHz and 16 – 30 GHz simultaneously. At 110 Myr (green solid lines) the predicted fluxes are slightly higher than the observed fluxes for 0.1 – 1 GHz, while the predicted fluxes are in good agreement with the observed fluxes for 1 – 30 GHz. We can conclude that the model spectra agree reasonably well with the observed spectrum of B1 relic reported by Stroe et al. (2016).

### 5. SUMMARY

We have performed time-dependent, DSA simulations of one-dimensional, spherical shocks, which sweep through the ICM thermal plasma with a population of relativistic electrons ejected from an AGN. In order to reproduce the observational data for B1 (head portion) of the Toothbrush relic, we adopt the following parameters:  $kT_1 \approx 5.9 - 6.9$  keV,  $M_{s,i} = 1.3 - 1.5$ ,  $u_{s,i} = 1.8 - 1.9 \times 10^3$  km s<sup>-1</sup>, and  $B_1 = 2$   $\mu$ G (van Weeren et al. 2016).

In addition, we assume that the preshock gas contains a pre-existing electron population of a power-law spectrum with the slope  $s = 0.6$  and exponential cutoff at  $\gamma_{e,c} = 7 - 8 \times 10^4$  as given in Equation (11). The power-law slope  $s$  is chosen to match the observed radio spectral index,  $\alpha_{\text{sh}} \approx 0.8$ , while  $\gamma_{e,c}$  is adopted to match the integrated radio spectrum of B1 relic for 1 – 30 GHz (Stroe et al. 2016). Note that the preshock region could be radio-luminous with the pre-existing electrons with such high  $\gamma_e$ . In the DSA models considered here, the synchrotron emissivity increases across the shock by a factor of 2.4 – 2.7 in the  $M_{s,i} = 1.3$  model and by a factor of 4.3 – 5.6 in the  $M_{s,i} = 1.5$  model.

After 110 Myr, the spherical shock slows down to  $M_s \approx 1.2 - 1.4$  with the postshock magnetic field strength  $B_2 \approx 2.5 - 2.8$   $\mu$ G. At this stage, the spatial profiles of the surface brightness,  $I_\nu$ , and the radio spectral index,  $\alpha_{0.15}^{0.61}$ , and the integrated radio spectrum,  $J_\nu$ , become consistent with the observations of B1 relic (van Weeren et al. 2016). Considering that the candidate source AGN is located about 200 kpc downstream of the shock (the northern edge of B1 relic) and there is no detectable radio fluxes in the preshock region, we suspect that the shock might have swept through the region permeated by relativistic plasma ejected from the source AGN.

The simple estimations for the widths of the downstream volume of radio emission behind a planar shock are about  $\Delta l_{\text{low}} \approx 120$  kpc at 150 MHz and  $\Delta l_{\text{high}} \approx 78$  kpc at 610 MHz at the shock age of 110 Myr. On the other hand, the width of the projected surface brightness of a spherical shell depends on the projection angles as shown in Figure 2. The observed profiles of radio fluxes at both frequencies can be modeled with the projection angles,  $\psi_1 = 15^\circ$  and  $\psi_2 = 23^\circ$ , as shown in Figure 5. So the arc-like radio-emitting shell is likely to be tilted slightly with respect to the sky plane as shown in the case (a) of Figure 2.

### ACKNOWLEDGMENTS

This research was supported by Basic Science Research Program through the National Research Foundation of Korea (NRF) funded by the Ministry of Education (2014R1A1A2057940). The author thanks R. J. van Weeren for providing the radio flux data for the Toothbrush relic published in van Weeren et al. (2016).

### REFERENCES

- Akamatsu, H., & Kawahara, H. 2013, Systematic X-Ray Analysis of Radio Relic Clusters with Suzaku PASJ, 65, 16
- Brüggen, M., Bykov, A., Ryu, D., & Röttgering, H. 2012, Magnetic Fields, Relativistic Particles, and Shock Waves in Cluster Outskirts Space Sci. Rev., 166, 187
- Brunetti, G., & Jones, T. W. 2014, Cosmic Rays in Galaxy Clusters and Their Nonthermal Emission, Int. J. of Modern Physics D, 23, 30007
- Clarke, T. E., Randall S. W., Sarazin, C. L., et al. 2013, Chandra View of the Ultra-Steep Spectrum Radio Source in A2443: Merger Shock-induced Compression of Fossil Radio Plasma ? ApJ, 772, 84
- de Gasperin, F., Ogrean, G. A., van Weeren, R. J., et al. 2015, Abell 1033: Birth of a Radio Phoenix, MNRAS, 448, 2197
- Drury, L. O'C. 1983, An Introduction to the Theory of Diffusive Shock Acceleration of Energetic Particles in Tenuous Plasmas, Rept. Prog. Phys., 46, 973
- Ensslin, T. A. 1999, Radio Ghosts, in Ringberg Workshop on Diffuse Thermal and Relativistic Plasma in Galaxy Clusters, ed. P. S. H. Böhringer, L. Feretti, vol. 271 of MPE Report, 275
- Ensslin, T. A., Biermann, P. L., Kleing, U., & Kohle S. 1998, Cluster radio relics as a tracer of shock waves of the large-scale structure formation, A&Ap, 332, 395
- Ensslin, T. A., & Brüggen, M., 2002, On the formation of cluster radio relics, MNRAS, 331, 1011
- Ensslin, T. A., & Gopal-Krishna, 2001, Reviving fossil radio plasma in clusters of galaxies by adiabatic compression in environmental shock waves A&Ap, 366, 26
- Feretti, L., Giovannini, G., Govoni, F., & Murgia, M. 2012, Clusters of galaxies: observational properties of the diffuse radio emission, A&A Rev, 20, 54
- Hong, E. W., Ryu, D., Kang, H., & Cen, R. 2014, Shock Waves and Cosmic Ray Acceleration in the Outskirts of Galaxy Clusters, ApJ, 785, 133
- Itahana, M., Takizawa, M., Akamatsu, Hi, et al. 2015, Suzaku observations of the galaxy cluster 1RXS J0603.3+4214: Implications of particle acceleration processes in the Toothbrush radio relic, PASJ, 67, 113
- Kang, H. 2011, Energy Spectrum of Nonthermal Electrons Accelerated at a Plane Shock, JKAS, 44, 49
- Kang, H. 2015a, Nonthermal Radiation from Relativistic Electrons Accelerated at Spherically Expanding shocks, JKAS, 48, 9
- Kang, H. 2015b, Radio Emission from Weak Spherical Shocks in the Outskirts of Galaxy Clusters, JKAS, 48, 39
- Kang, H., & Jones, T. W. 2006, Numerical Studies of Diffusive Shock Acceleration at Spherical Shocks, Astropart. Phys., 25, 246
- Kang, H., & Ryu, D. 2011, Re-acceleration of Non-thermal Particles at Weak Cosmological Shock Waves, ApJ, 764, 95



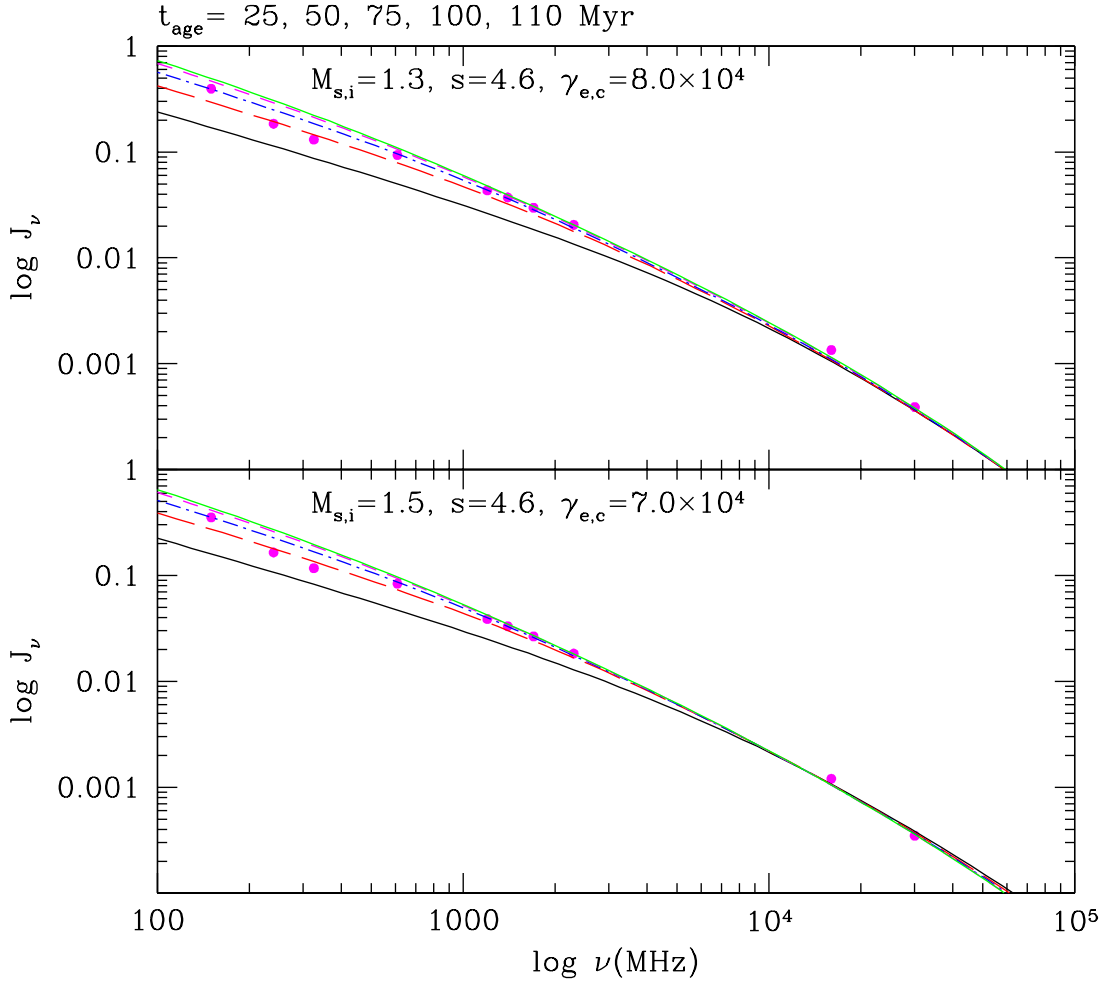


**Figure 6.** Time evolution of volume-integrated radio spectrum for the shock models with  $M_{s,i} = 1.3$  (top panels) and  $M_{s,i} = 1.5$  (bottom) at  $t_{\text{age}} = 25$  (black solid lines), 50 (red long-dashed), 75 (blue dot-dashed), 100 (magenta dashed), and 110 Myr (green solid). The magenta dots are the observational data taken from Table 3 of Stroe et al. (2016).

Kang, H., & Ryu, D. 2015, Curved Radio Spectra of Weak Cluster Shocks, *ApJ*, 809, 186  
 Kang, H., & Ryu, D. 2016, Re-acceleration Model for Radio Relics with Spectral Curvature, *ApJ*, in press  
 Kang, H., Ryu, D., & Jones, T. W. 2012, Diffusive Shock Acceleration Simulations of Radio Relics, *ApJ*, 756, 97  
 Kang, H., Vahe, P., Ryu, D., & Jones, T. W. 2014, Injection of  $\kappa$ -like Suprathermal Particles into Diffusive Shock Acceleration, *ApJ*, 788, 141  
 Kempner, J. C., Blanton, E. L., Clarke, T. E., et al. 2004, Conference Note: A Taxonomy of Extended Radio Sources in Clusters of Galaxies, in *The Riddle of Cooling Flows in Galaxies and Clusters of galaxies*, ed. T. Reiprich, J. Kempner, & N. Soker, 335  
 Ogrean, G. A., Brüggén, M., van Weeren, R., Röttgering, H., Croston, J. H., & Hoeft, M. 2013, Challenges to our understanding of radio relics: X-ray observations of the Toothbrush cluster, *MNRAS*, 433, 812  
 Pinzke, A., Oh, S. P., & Pfrommer, C. 2013, Giant radio relics in galaxy clusters: re-acceleration of fossil relativistic electrons?, *MNRAS*, 435, 1061  
 Russell, H. R., van Weeren, R. J., Edge, A. C. et al., 2011 A merger mystery: no extended radio emission in the

merging cluster Abell 2146, *MNRAS*, 417, L1  
 Ryu, D., Kang, H., Hallman, E., & Jones, T. W. 2003, Cosmological Shock Waves and Their Role in the Large-Scale Structure of the Universe, *ApJ*, 593, 599  
 Sarazin, C. L. 1988, *X-ray Emission from Clusters of Galaxies*, Cambridge University Press, Cambridge  
 Shimwell, T. W., Markevitch, M., Brown, S., Feretti, L, et al., 2015, Another shock for the Bullet cluster, and the source of seed electrons for radio relics, *MNRAS*, 449, 1486  
 Skilling, J. 1975, Cosmic Ray Streaming. I - Effect of Alfvén Waves on Particles, *MNRAS*, 172, 557  
 Skillman, S. W., Hallman, E. J., O’Shea, W., Burns, J. O., Smith, B. D., & Turk, M. J. 2011, Galaxy Cluster Radio Relics in Adaptive Mesh Refinement Cosmological Simulations: Relic Properties and Scaling Relationships, *ApJ*, 735, 96  
 Slee O. B., Roy A. L., Murgia M., Andernach H., & Ehle M., 2001, Four Extreme Relic Radio Sources in Clusters of Galaxies, *AJ*, 122, 1172  
 Stroe, A., Shimwell, T. W., Rumsey, et al. 2016, The widest frequency radio relic spectra: observations from 150 MHz to 30 GHz, *MNRAS*, 455, 2402

- Trasatti, M., Akamatsu, H., Lovisari, L., Klein, U., Bonafede, A., Brüggén, M., Dallacasa, D. & Clarke, T. 2015, The radio relic in Abell 2256: overall spectrum and implications for electron acceleration, *A&Ap*, 575, A45
- van Weeren, R., Brunetti, G., Brüggén, M. et al. 2016, LO-FAR, VLA, and CHANDRA Observations of the Toothbrush Galaxy Cluster, *ApJ*, 818, 204
- van Weeren, R., Röttgering, H. J. A., Brüggén, M., & Hoeft, M. 2010, Particle Acceleration on Megaparsec Scales in a Merging Galaxy Cluster, *Science*, 330, 347
- van Weeren, R. J., Röttgering, H. J. A., & Brüggén, M. 2011b, Diffuse steep-spectrum sources from the 74 MHz VLSS survey, *A&AP*, 527, A114
- van Weeren, R., Röttgering, H. J. A., Intema, H. T., Rudnick, L., Brüggén, M., Hoeft, M., & Oonk, J. B. R. 2012, The “Toothbrush-relic”: evidence for a coherent linear 2-Mpc scale shock wave in a massive merging galaxy cluster?, *A&AP*, 546, 124
- Vazza, F., Brunetti, G., & Gheller, C. 2009, Shock waves in Eulerian cosmological simulations: main properties and acceleration of cosmic rays, *MNRAS*, 395, 1333